

This open access document is posted as a preprint in the Beilstein Archives at https://doi.org/10.3762/bxiv.2025.61.v1 and is considered to be an early communication for feedback before peer review. Before citing this document, please check if a final, peer-reviewed version has been published.

This document is not formatted, has not undergone copyediting or typesetting, and may contain errors, unsubstantiated scientific claims or preliminary data.

Preprint Title Ultrasonic Irradiation in the Synthesis of Nanohydroxyapatite: A

Chemically Friendly Technique for Improving Hemocompatibility and

Antibiofilm Applications

Authors Juan Mendoza Turmero, Cristina Parra Pantoja, Marcos Sabino

Gutiérrez, Milagro Fernández-Delgado, Claudia Alvarado-Castillo, Damarys Soto Gil, María E. Gomes Gomes, Yoni Gutiérrez Barrios

and Daniel Suárez Arteaga

Publication Date 05 Nov 2025

Article Type Full Research Paper

Supporting Information File 1 Section I-General assignment of infrared bands.docx; 19.6 KB

Supporting Information File 2 Section II-Histograms with hydroxyapatite particle sizes.docx; 211.7

KΒ

ORCID® iDs Juan Mendoza Turmero - https://orcid.org/0009-0007-3015-8414;

Cristina Parra Pantoja - https://orcid.org/0009-0004-1190-7449;

Marcos Sabino Gutiérrez - https://orcid.org/0000-0001-8316-7241;

Milagro Fernández-Delgado -

https://orcid.org/0000-0001-6111-1116; Claudia Alvarado-Castillo -

https://orcid.org/0000-0002-1352-2524; Damarys Soto Gil -

https://orcid.org/0009-0006-2613-7672; María E. Gomes Gomes - https://orcid.org/0009-0005-2440-1794; Yoni Gutiérrez Barrios -

https://orcid.org/0009-0008-4681-1446; Daniel Suárez Arteaga -

https://orcid.org/0009-0007-2036-9664



License and Terms: This document is copyright 2025 the Author(s); licensee Beilstein-Institut.

Ultrasonic Irradiation in the **Synthesis** of

Nanohydroxyapatite: Chemically Α Friendly

Technique for Improving Hemocompatibility

Antibiofilm Applications

Juan Mendoza Turmero¹, Cristina Parra Pantoja*², Marcos Sabino Gutiérrez³, Milagro

Fernández-Delgado⁴, Claudia Alvarado-Castillo⁵, Damarys Soto Gil⁶, María E. Gomes

Gomes², Yony Gutiérrez Barrios⁴, Daniel Suárez Arteaga⁵.

¹ Department of Materials Science, Simón Bolívar University, Caracas, Venezuela.

² Functional Nanostructured Materials Laboratory, Center for Materials Engineering

and Nanotechnology, Venezuelan Institute for Scientific Research (IVIC). Miranda

State, Venezuela.

³ Department of Chemistry, B⁵ida Group, Simón Bolívar University, Caracas,

Venezuela.

Bionanotechnology Laboratory, Engineering Center for Materials and

Nanotechnology, IVIC. Miranda State, Venezuela.

⁵ Laboratory of Hemostasis and Vascular Genetics, Center for Biophysics and

Biochemistry, IVIC. Miranda State, Venezuela.

⁶ Nanomaterials Characterization Laboratory, Center for Materials Engineering and

Nanotechnology, IVIC. Miranda State, Venezuela.

Email: Cristina Parra Pantoja* – cpantojave@gmail.com

* Corresponding author

1

Abstract

This study explores the synthesis of nanohydroxyapatite (nHA) using high-frequency ultrasonic irradiation (UI), a chemically friendly technique aligned with green chemistry principles. Synthesis was achieved by varying the UI time (15, 30, 45, and 60 minutes) and the reaction medium. Water-based mixtures were used: water/acetone (W/ACET), water/tetrahydrofuran (W/THF), and water/ethanol (W/ETOH). The resulting nHA was characterized structurally using FTIR, XRD, TGA, and SEM. These analyses revealed the formation of carbonated nHA similar to biological apatite, with distinct morphologies and particle sizes dependent on the solvent used. All synthesized materials exhibited high thermal stability and yields exceeding 80%. Hemocompatibility studies showed that nHA samples obtained in the W/THF mixture presented low hemotoxicity (1-2 % hemolysis), and did not affect platelet ADP aggregation processes. Microbiological assays showed a significant reduction in P. aeruginosa biomass production (p<0.05) after 24 hours, particularly for nHA synthesized with the W/ETOH mixture. There was also a less bacterial colonization, cellular aggregates or formation of specialized structures when was treated with this bioceramic, compared to the commercial hydroxyapatite, suggesting potential antibiofilm properties. This research presents an original and efficient method for producing nHA as a promising biomaterial for tissue engineering and bone replacement applications.

Keywords

antibiofilm properties; hemocompatibility; nanohydroxyapatite; ultrasonic irradiation

Introduction

Nowadays, there is a high demand for the development of bone substitutes that are biocompatible, bioactive, mechanically strong, and well-tolerated by the immune system [1], which represents a major challenge for science. Prostheses used to repair skeletal system defects and diseases should be customized devices to respond specifically physiological demands of each organism different [2, 3, 4]. For this reason, the most recent research shows a trend toward biomimicry, or the use of materials with structures and properties very similar to those of biological origin [5]. This process involves reaching nanodimensions and reproducing the monolithic structure of bone [6], which has been difficult to achieve until now. Bones are complex system, composed of hydroxyapatite crystals in the form of nanoneedles, that are closely bound together with type I collagen fibrils [7], as shown in Figure 1.

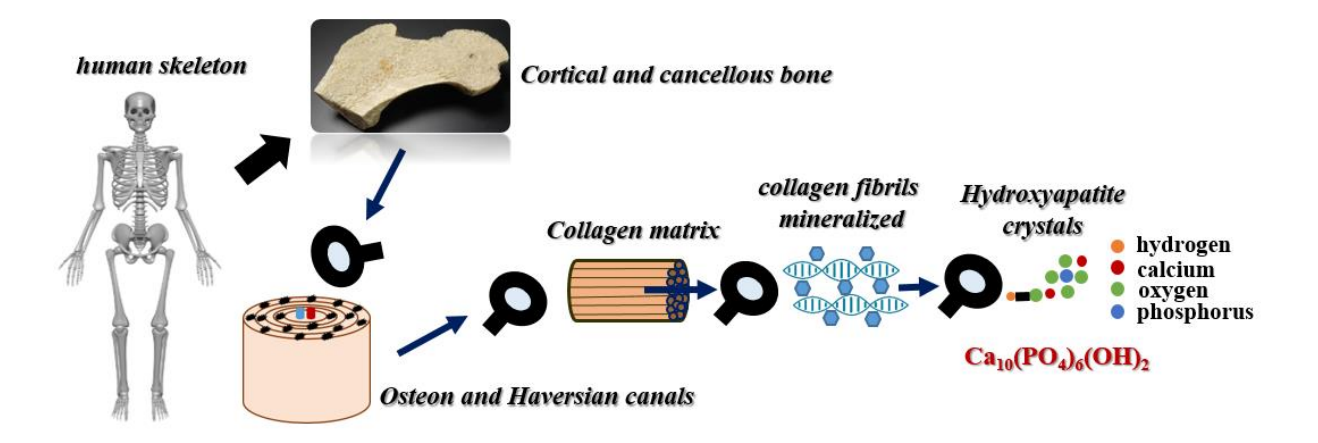


Figure 1: The Hierarchical structure of the human skeletal system. The image of "human skeleton" was reproduced from https://pixabay.com/es/illustrations/esqueleto-humano-huesos-cr%c3%a1neo-1158318/ by TymonOziemblewski via Pixabay and the image of "Cortical and cancellous bone" has been reproduced from

https://pixabay.com/es/photos/eldetalle-de-los-huesos-4451356/ by MAKY_OREL via Pixabay. This content is not subject to CC BY 4.0.

Hydroxyapatite crystals are important source of calcium and phosphorus, which give bone its density, mechanical strength, and bioactivity [8]. Methods for obtaining nHA can be grouped into five categories: i) wet methods, ii) dry methods, iii) high-temperature processes, iv) from biogenic sources, v) with high-energy sources [9,10]. The resulting hydroxyapatite is used for bone scaffolds and fillers [11], devices for controlled drug release [12], and implant coatings [13]. The most widely reported method for obtaining hydroxyapatite is the hydrothermal method [14]. However, this synthesis procedure involves high energy consumption due to the high temperatures required and prolonged reaction times [15]. Figure 2 summarizes some of the advantages and disadvantages of each synthesis method.

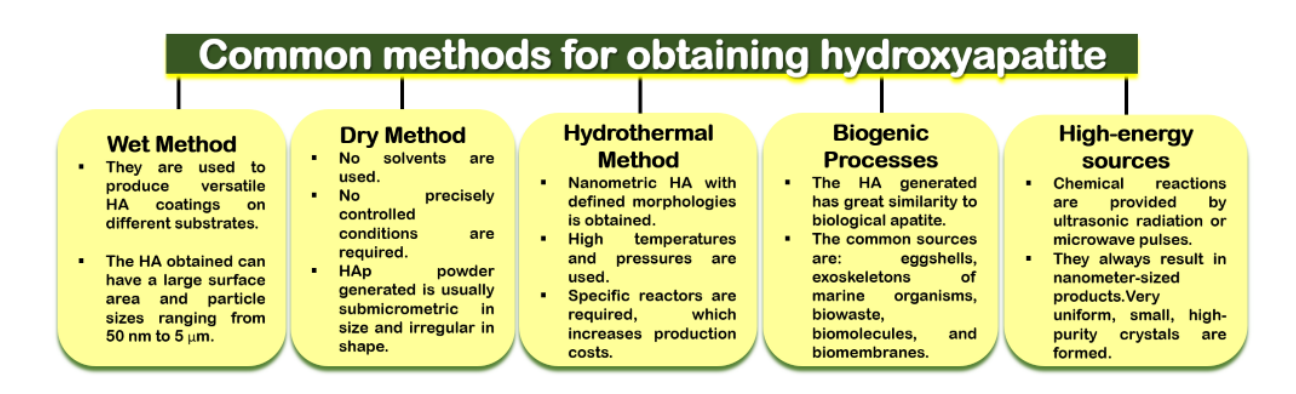


Figure 2: Advantages and disadvantages of the main methods for obtaining hydroxyapatite.

To propose alternative methodologies to those mentioned in Figure 2, we implemented low energy consumption techniques that allow for ease in handling reaction variables. One of the novelest and versatile processes for obtaining hydroxyapatite is sonochemistry which uses high-frequency ultrasound as an energy source [16]. Sonochemistry shows great potential and has therefore aroused significant interest. This is because the chemical effects of ultrasound do not originate from a direct

interaction between sound waves and the molecular species present in the medium. Rather, they derive mainly from the physical phenomenon called acoustic cavitation, a physical phenomenon that efficiently concentrates diffuse sound energy and is much more powerful than common thermal energy transfer.

When high-frequency sound waves pass through a liquid medium, a large number of microbubbles form, grow, and collapse within intervals as short as a few microseconds. According to sonochemical theory calculations, and experimental evidence, have indicated that this process can generate local temperatures as high as 3000 K and local pressures as high as 1000 atm, heating and cooling the medium at rates as high as 10⁹K/s [16]. In this harsh reaction environment, ions, free radicals, and other highly reactive chemical species are easily generated without the need for reaction initiators. For this reason, ultrasonic irradiation is widely used in the formation, grinding, dispersion, and activation of many inorganic compounds at the micro and nanoscale [17,18].

Previous research has reported, the production of carbonated hydroxyapatite, which has a structure very similar to that of biological apatite, has been reported using high-frequency ultrasound [19]. Due to the complexity of the physicochemical processes that occur in the medium during sonochemical synthesis, the resulting particles can exhibit great variability in morphology. These particles can be in the form of needles, regular and irregular spheres, rods, and many others [20,21]. They also exhibit high degrees of crystallinity, high purity, and nanoscale dimensions [22]. The fascinating properties of the resulting material have led to very promising results, further diversifying its multiple applications [23]. Some studies have also shown that synthesis parameters such as the type of solvent, ultrasonic irradiation time, and the nature of the reactants used as nHA precursors, directly influence the microstructure of the resulting material [24]. Due to the simplicity of the reaction medium, low energy

consumption, and short processing times required to obtain the products, nHA synthesis carried out with ultrasonic irradiation complies with the precepts of green chemistry [25]. Green chemistry involves designing of chemical processes and products that reduce or eliminate the use and generation of hazardous substances, through a sustainable approach, that meets current needs without compromising the availability of resources and the quality of life of future generations [26]. Nanohydroxyapatite is distinguished by its remarkable osteoinduction and osteoconduction capabilities, making it a bioceramic with great potential in biomedical engineering. Its low hemotoxicity [27,28] and antibacterial properties [29,30] further expand its applicability in the field of biomaterials. It is also important to determine the antibiofilm effectiveness of this bioceramic against opportunistic bacteria such as Pseudomonas aeruginosa. This pathogen is responsible for high rates of morbidity, mortality as well as multi-drug resistance, worldwide [31]. A key factor in its pathogenicity and transmission is its ability to form virulent biofilms, which are particularly difficult to eradicate. Biofilms are communities of microbial cells enclosed by exopolysaccharides (EPS) that adherent to an inert or living surfaces. These biofilms enhance bacterial growth and survival by providing access to nutrients and protection against toxic compounds, adverse environmental conditions, antimicrobials and the host immune response [32]. Biofilms are a critical virulence factors for many bacterial pathogens that can cause chronic infections, accounting for more than 80% of human microbial infections. P. aeruginosa biofilms are given view of this, P. aeruginosa has been considered a model for studying for nosocomial bacterial biofilms [33,34], more effective biofilm control strategies should be developed for patients requiring indwelling medical devices.

Thanks to its multifunctionality and excellent bioactive and biocompatible properties, the synthesis, characterization, and study of hydroxyapatite continue to provide significant advantages in the development of new biomaterials. Furthermore, obtaining nHA through a green chemistry approach adds to its many existing advantages. Based on these premises, this study investigated the influence of ultrasonic irradiation on hydroxyapatite properties by varying the irradiation time and solvents used in the synthesis process. Additionally, we evaluated their hemocompatibility and ability to inhibit colonization or biofilm formation against pathogens, contributing to the exploration of new nHA-based biomaterials for use in tissue engineering and bone devices.

Results and Discussion

Infrared study (FTIR)

Figure 3 shows the FTIR spectra of hydroxyapatite prepared using mixtures of W/ACET, W/THF, and W/ETOH with varying UI times between 15 and 60 min. The spectra in Figures 3 (A), (B), and (C), show the characteristic absorption bands of the hydroxyapatite structure can be seen [35, 36]: the presence of OH groups in the ranges (3573-3558) cm⁻¹ and (633-628) cm⁻¹ is verified, as are the vibrational modes of PO₄⁻³ ions [v₁: 963-962, v₂: 476-471, v₃: 1097-1038, and v₄: 603-656] cm⁻¹.

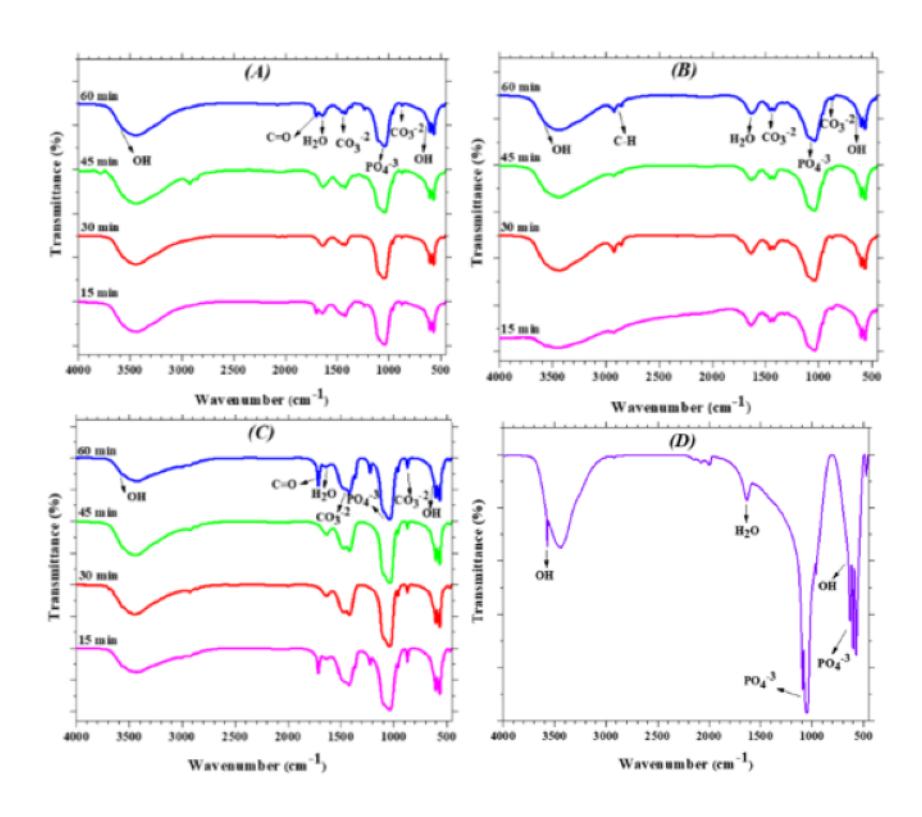


Figure 3: FTIR spectra of nHA obtained in: (A) W/ACET, (B) W/THF, and (C) W/ETOH at 15, 30, 45, and 60 minutes of UI, (D) Commercial Hydroxyapatite.

The Remaining bands in the spectra shown in the spectra in Figure 4 indicate the presence of carbonate groups within the wave number ranges of [v2: 875-873; v3: 1499-1420] cm⁻¹. This certifies that, carbonated hydroxyapatite was obtained under all synthesis conditions [37]. Additional absorption bands observed in most of the spectra in Figure 4 correspond to carbonyl group vibrations between 1739-1701 cm⁻¹, and to the adsorbed water molecules at 1636 cm⁻¹ (nHA obtained in the W/ACET system), 1634 cm⁻¹ (nHA obtained in the W/THF system), and (1638-1634) cm⁻¹ (nHA obtained in the W/ETOH system).

Table A (shown in Section 1, as supplementary information), systematically summarizes the assignment of absorption bands for the PO_4^{-3} and OH^- ions, as well as for the v_3 and v_2 vibrational modes of the CO_3^{-2} ions. This is compared with a sample of non-carbonated commercial hydroxyapatite from Teknimed S.A. in France, which is used as a reference. The versatile structure of hydroxyapatite the replacement of its

constituent chemical species (calcium ions, phosphates, and hydroxyls) [38, 39]. This substitution process produces changes in its properties, including crystallinity, morphology, and lattice parameters [40, 41]. The nHA obtained using the three aforementioned mixtures as solvents exhibited type A, B, and AB substitutions in its structure. Type B substitution (when carbonates occupy the PO₄-3 sites) [42, 43], is particularly evident due to significant shifts observed in the v₃ vibrational modes (doublet of the PO₄-3 group) of the synthesized samples compared to the commercial hydroxyapatite sample. This change is also evident in the more pronounced width of the bands corresponding to the phosphate doublets (Figures 3-A, 3-B, and 3-C) when compared to the same absorption band in Figure 4-D. It is important to note that the intensity of the v₃ band which corresponds to type B substitution, and appears in all the spectra in Figure 4, in the range of (1424-1420 cm⁻¹), is more pronounced than that of those of type A, (1499-1493 cm⁻¹), which occupies the OH sites. This confirms that for these syntheses, the substitution effect was much greater at the phosphate sites than at the hydroxyl sites. According to the literature, replacing phosphate ions is difficult because they are strongly bound to calcium cations within the hydroxyapatite structure. Replacing phosphates with other anions, such as carbonate, significantly alter the properties of this bioceramic, resulting in decreased hardness and stability [44]. However, high-frequency ultrasound provides enough energy to promote this process, which would likely be more difficult using other synthesis methods [45]. Type A substitution (carbonates for hydroxyls) was only observed in nHA obtained from W/ACET and W/THF mixtures, and was not observed in nHA synthesized using W/ETOH as a solvent. These results suggest that the free OH ions in hydroxyapatite are more strongly bound to its structure, making them very unlikely to leave it, even in a more highly polar medium such as that provided by the W/ETOH mixture [46].

Incorporating polyatomic anions such as carbonate into the hydroxyapatite structure creates vacancies and calcium deficiencies, which lead to the formation of a non-stoichiometric hydroxyapatite with a hexagonal structure and space group P6₃/m [47]. Table 2 shows the Ca/P ratios determined by EDX analysis of nHA samples synthesized at 15 and 60 minutes of ultrasonic irradiation in W/ACET, W/THF, and W/ETOH mixtures. According to the results shown in Table 1, the HA obtained in the W/ACET mixture was calcium deficient at low ultrasonic irradiation times, while that obtained in W/THF was stoichiometric. This occurs because the substitution of carbonate for phosphate and hydroxyl results in non-stoichiometric HA, accounting for the variations in the Ca/P ratio.

Table 1: Ca/P ratios determined from EDX analysis of nHA samples synthesized at 15 and 60 minutes of UI using W/ACET, W/THF, and W/ETOH mixtures.

Sample	Solvent	UI Time (min)	Ca (wt %)	P (wt %)	Ca/P ratio
	W/ACET	15	9.20	5.89	1.56
		60	12.14	6.5	1.87
nHA	W/THF	15	18.20	11,22	1.62
ППА	VV/ I [][60	9.44	5.79	1.63
	W/ETOH	15	16.85	8.35	2.02
		60	3.36	1.58	2.13

On the other hand, the HA formed using W/ETOH as a solvent was also not stoichiometric, but unlike that prepared in W/ACET, it was obtained with an excess of calcium. These results demonstrate the significant influence of the solvent type and UI time on the formation of nHA that is similar to or different from biological apatite. Similar

findings have been reported by other authors using different synthesis methods [48, 49]. Another important result is the appearance of bands associated with the carbonyl group in some of the FTIR spectra of the synthesized nHA at certain ultrasonic irradiation times. The W/ACET and the W/ETOH mixtures (15 and 60 minutes of UI), W/THF mixture (15 and 30 minutes of UI) exhibited this phenomenon. This suggests that the high energy capacity of ultrasonic waves promotes, in the reaction medium, the formation and coexistence of another distinct mineral phase with which has carbonate groups in its composition. Table 2 shows the carbonate content of the nHA samples, which was calculated by integrating the absorption bands in the v_3 region of the CO_3^{-2} ions, in all nHA spectra, in the range (1560-1380) cm⁻¹. These results indicate that the variation in the content of these ions, in relation to the solvent mixture used in the synthesis, would as follows: W/ETOH > W/ACET \approx W/THF.

Table 2: Peak area determined from the FTIR spectra of nHA, for the v_3 vibrational modes of carbonate ions (1560-1380 cm⁻¹).

Solvent	UI Time (min)	Area CO ₃ -2
	15	15.75
W/ACET	30	9.21
	45	23.28
	60	9.27
	15	15.71
W/THF	30	12.49
VV/ 1111	45	12.54
	60	17.54
	15	47.92
W/ETOH	30	35.16
VV/ETON	45	34.64
	60	42.86

The spectra of the nHA samples obtained in the W/ETOH mixtures (Figure 3-C), show intense and well-defined carbonate bands, particularly for the nHA prepared at 15 and 60 minutes of ultrasonic irradiation. This is consistent with the results shown in Table 2. Furthermore, the spectra in Figures 3-A and 3-C show the presence of a carbonyl band at 1712 and 1726 cm⁻¹, for the 15 and 60 minutes of ultrasonic irradiation, respectively, indicating an additional contribution of carbonate groups in both spectra.

X-ray diffraction (XRD)

Figure 4 shows the X-ray diffractograms of the nHA obtained from the W/ACET, W/THF, and W/ETOH mixtures at various UI times. Almost all of the diffraction peaks shown in Figures 4-A, 4-B, and 4-C correspond to those reported in the literature for hydroxyapatite [50,51]. The main diffraction peak corresponding with the highest intensity appears at approximately $2\theta = 31.70^{\circ}$, followed by three adjacent peaks at 2θ = 32.20°, 2θ = 32.90°, and 2θ = 34.22°. These results correspond to what was observed by FTIR regarding the formation of a carbonated hydroxyapatite with a hexagonal crystalline structure [52,53]. Additionally, other crystallographic planes such as (212), (130), (302), (222), (213), (321), (140), (402), and (004), are very similar to those reported for biological apatite or apatite derived from biogenic according to previous studies [54, 55]. The pronounced width of all the diffraction peaks in Figures 4-A and 4-B could indicate an appreciable decrease in particle size of the obtained hydroxyapatite by increasing the ultrasonic irradiation time in the reaction medium [56, 57]. Regarding to the reactions in the W/ETOH mixture, rhombohedral calcite formation (space group R3c) was confirmed by a well-defined signal at $2\theta = 29.20^{\circ}$ appearing in the diffractograms corresponding to 15 and 60 minutes of ultrasonic irradiation (Figure 4-C). This signal corresponds to the highest-intensity calcite peak, plane (104), in accordance with reference pattern 00-002-0629 from the JCPDS database. These results were corroborated by those obtained via infrared spectroscopy, as shown in Figure 3-C.

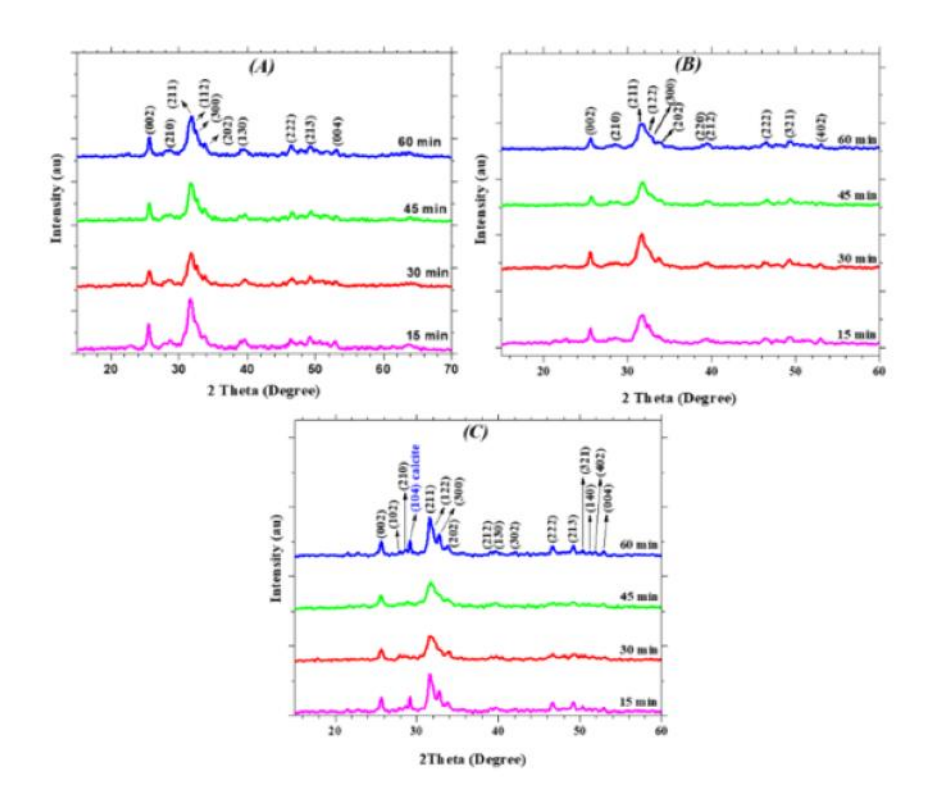


Figure 4: X-ray diffractograms of nHA synthesized in the mixtures: (A) W/ACET, (B) W/THF, and (C) W/ETOH; at 15, 30, 45, and 60 minutes of UI.

The phenomenon of ultrasonic cavitation, within a polar medium such as a W/ETOH mixture, facilitates the formation of ionic species that are susceptible to rapid recombination processes, giving rise to a more stable crystalline phase. According to the literature that the Gibbs free energy change (Δ Gf) for the formation of hydroxyapatite is -12.677 kJ/mol [58], and for calcite it is -1.128 kJ/mol [59]. The larger numerical value of Δ Gf (hydroxyapatite) with a negative sign implies greater thermodynamic stability compared to the calcite phase. This is associated with the greater ease of hydroxyapatite formation. This explains why calcite and hydroxyapatite formed in the presence of the W/ETOH mixture, which is effective for solvating the formed species, and the extraordinary energy provided by high-frequency ultrasound. The calcite formed in greater proportion at 60 minutes and the hydroxyapatite formed

in lesser proportion at 15 minutes of irradiation. This is evident from the higher carbonate content of the samples obtained at these two times (Table 2), those obtained at intermediate irradiation times (30 and 45 minutes). To definitively confirm calcite formation in the syntheses conducted in the W/ETOH mixture, samples obtained at 15 and 60 minutes of ultrasonic irradiation were calcined at 1100 °C in air, and resulting product was studied using infrared and X-ray diffraction. Figure 5-A shows that, after calcination, the carbonyl band disappears for the solid obtained at 15 minutes and the bands associated with the carbonate groups decrease significantly. In contrast, the bands of both functional groups (C=O and CO₃²⁻) remain in the FTIR spectrum of the sample synthesized at 60 minutes of UI. This behavior is associated with the formation of different proportions of calcite at 15 and 60 minutes of reaction (see Figures 5-B and 5-C).

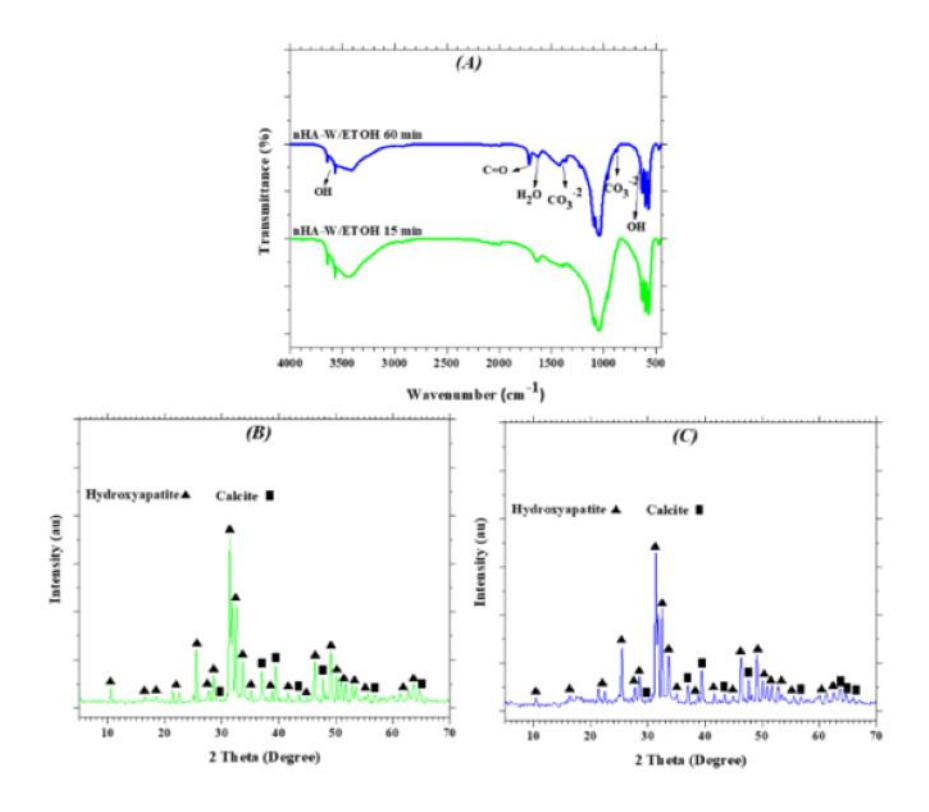


Figure 5: (A) FTIR spectra of the calcination residue of nHA obtained in the W/ETOH at 15 and 60 min of UI, (B) and (C) X-ray diffractograms of the calcination residue of nHA obtained at 15 and 60 min of UI.

These results, along with those from FTIR, demonstrate that the sonication energy was able to promote the joint precipitation of both crystalline phases in both reactions carried out at 15 and 60 minutes of UI. Results shown by Kitamura et al [60] revealed that the dissolution of calcium hydroxide in the reaction medium can significantly influence the nucleation of certain calcium carbonate polymorphs. In this sense, the solubility product (Ksp) is a parameter that can help predict the formation and/or dissolution of solids. For Ca(OH)₂ in an aqueous solution, this constant has a value of (5.5×10^{-6}) [61], compared to the Ksp of CaCO₃ (3.3×10^{-9}) [61], which is much smaller. This significant difference may explain why calcite forms more easily at the expense of Ca(OH)2, which is more soluble and thus more readily available in the reaction medium. Some authors have reported that the main decomposition products when a medium containing alcohol is subjected to ultrasonic irradiation, the main decomposition products are hydrogen, methane, ethylene, aldehydes, and carbon monoxide [62]. In this study, some of the reactions to obtain nHA were carried out in a W/ETOH medium subjected to high-frequency ultrasound. Therefore, the following sequence of chemical reactions could reasonably justify the formation of calcite:

$$CH_3 CH_2 OH \rightarrow CH_3 \dot{C}H_2 + \dot{O}H \tag{1}$$

$$\dot{O}H + CH_3CH_2OH \rightarrow CH_3\dot{C}HOH + H_2O$$
 (2)

$$CH_3\dot{C}H_2 + CH_3CH_2OH \rightarrow CH_3\dot{C}HOH + CH_3CH_3$$
 (3)

$$CH_3\dot{C}HOH \rightarrow CH_3COH + \dot{H}$$
 (4)

$$CH_3COH + \dot{O}H \rightarrow CH_3\dot{C}O + H_2O$$
 (5)

$$CH_3\dot{C}O + H \rightarrow C\dot{H}_4 + CO \tag{6}$$

$$CO_{(g)} + H_2O_{(l)} \rightleftharpoons CO_{2(g)} + H_{2(g)}$$
 (7)

$$CO_{2(g)} \rightleftharpoons CO_{2(aq)} \tag{8}$$

$$CO_{2(aq)} + H_2O_{(l)} \rightleftharpoons H_2CO_{3(aq)}$$
 (9)

$$H_2CO_{3(aq)} \rightleftharpoons HCO_{3(aq)}^- + H_{(aq)}^+$$
 (10)

$$HCO_{3(aq)}^{-} \rightleftharpoons CO_{3}^{-2} + H_{(aq)}^{+}$$
 (11)

The transformation can occur very quickly due to the presence of calcium hydroxide and carbonate ions in the reaction medium:

$$Ca(OH)_{2(s)} \rightleftharpoons Ca_{(aq)}^{+2} + 2OH_{(aq)}^{-}$$
 (12)

$$Ca_{(aq)}^{+2} + CO_3^{-2} \rightarrow CaCO_{3(s)}$$
 (13)

The solubility product of hydroxyapatite is a key a parameter of great interest for understanding its higher precipitation capacity compared to calcite. An acceptable value for the Ksp of HA is 2.91×10^{-58} , as reported by L. C. Bell et al [63]. According to reaction 14, this value indicates the degree to which hydroxyapatite will dissolve in water or biological fluids at a specific temperature:

$$Ca_{10}(PO_4)_6(OH)_{2(s)} \rightleftharpoons 10 Ca_{(aq)}^{+2} + 6 PO_{4(aq)}^{-3} + 2 OH^-$$
 (14)

The equilibrium constant for the dissolution reaction of HA in a saturated solution is given by the expression shown in expression 15:

$$K_{sp} = [Ca^{+2}]^5 * [PO_4^{-3}]^3 * [OH^-]^2 = 3.37 \times 10^{-58}$$
 (15)

This low solubility is vital in biological systems such as bones and teeth, where hydroxyapatite provides a stable, insoluble reserve of calcium and phosphate ions. Its use in various applications of interest to this research, such as bone grafts and coatings, is also relevant. In these applications, the slow dissolution rate is a desirable property.

Yield in the ultrasonic synthesis of hydroxyapatite

Figure 6 shows the experimental yields obtained from the synthesis of nHA using different solvent mixtures and UI times (15, 30, 45, and 60 min). The performance

values ranged from 78% to 97%, the highest yields were observed in the W/ACET mixture and the lowest were observed in the W/ETOH mixture.

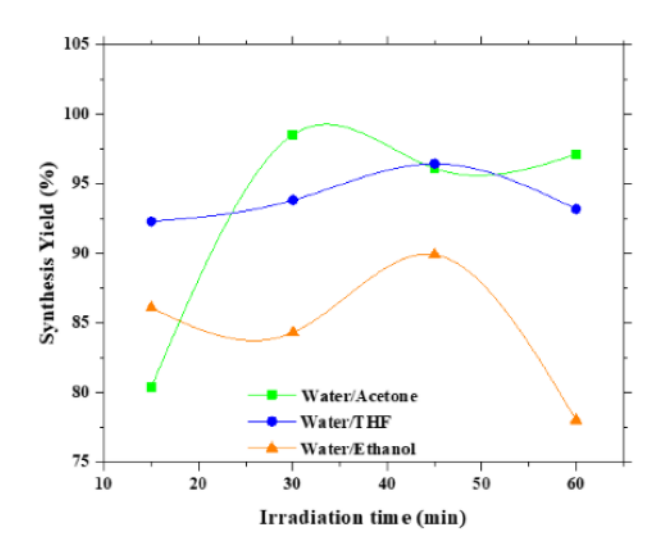


Figure 6: Yields obtained in the synthesis of hydroxyapatite, carried out in W/ACET, W/THF, and W/ETOH mixtures, at 15, 30, 45, and 60 min of UI.

The following order of effectiveness for nHA formation is established: W/ACET > W/THF > W/ETOH. This trend can be attributed to the dielectric constants [64], water solubility, and dipole moments of the solvent mixtures as shown in Table 3.

Table 3: Some physical constants of interest for water, THF, ethanol, and acetone

Mixture/Substance	€	μ	Solubility
Water/Acetone	50.40	-	-
Water/THF	44.29	-	-
Water/Ethanol	52.75	-	-
Water	80.10	1.82	-
Tetrahydrofuran	7.58	1.75	in water (s)
Acetone	20.70	2.85	in water (∞)
Ethanol	24.50	1.69	in water (∞)

$$\epsilon_{mixture} = \epsilon H_2 O \ x \ 0.5 + \epsilon_{solvent} \ x \ 0.5$$
 (16)

 $\in_{mixture:}$ Relative permittivity of the mixture (water + organic solvent)

μ: Dipole moment

(s): soluble

(∞): infinitely soluble

The W/ACET mixture was the most effective at promoting the separation, solvation, and stabilization of the Ca⁺², OH⁻, and PO₄⁻³ ions. This resulted in a higher recombination rate, resulting in the rapid formation of hydroxyapatite and, consequently, higher yields. In contrast, although the W/THF mixture, despite yielded values above 90%, it showed a decrease in synthesis yield. This was due to a notable drop in the mixture's dielectric constant and the dipole moment of THF, which reduced the nucleation rate of hydroxyapatite. A significant increase in polarity did not result in higher yields for the W/ETOH mixture. This is because the W/ETOH system has unique hydrogen bond interactions that limit the availability of active sites for the solvation of calcium, phosphate, and hydroxyl ions, which resulted in a notable decrease in the production yield of nHA. Other authors have reported similar results in the sol-gel synthesis of nHA. These results, however, were not performed with solvent mixtures. They provide clear evidence of the marked influence of the reaction medium on the production of hydroxyapatite in the presence of alcohols, ketones, and aprotic solvents such as tetrahydrofuran [65]. The ultrasonic irradiation time required to obtain these high yields was highly variable and significantly influenced overall process. This demonstrates that nHA can be prepared in shorter periods, than those used in conventional synthesis methods such as hydrothermal, precipitation and sol-gel, among others. For the W/THF mixtures, the optimum time for maximum yield was 30 minutes. Using W/ACET and W/ETOH, the maximum yields were achieved at 45 minutes of irradiation. These results conclusively demonstrate the wide range of possibilities for obtaining nHA with a highly energetic source, such as high-frequency ultrasound.

Thermal stability study by TGA

Figure 7 shows the thermograms of the nHA samples synthesized using W/ACET, W/THF, and W/ETOH mixtures. In general, the thermal decomposition process for samples obtained with W/ACET (Figure 7-A) and W/THF (Figure 7-B) occurs in one single stage, with a total mass loss ranging from 11% to 15%. almost half of this loss is attributed to the release of adsorbed water between 100 °C and 200 °C [66]. W/ACET Mixture: A second, gentle slope of mass loss is which is likely associated with the release of structural water between 400 °C and 600 °C. Furthermore, the slight change in observed slope around 400 °C for the 45 and 60 min samples, accompanied by a mass loss ranging from 0.5% and 0.7%, could be related to the initial stages of hydroxyapatite decarbonation [67]. W/THF Mixture: The sample that was synthesized after 15 minutes of ultrasonic irradiation had the highest total mass loss (12.62%). The curves for the 30 and 45 min are completely overlapping, which suggests that there are no significant changes in degradation behavior at these times. W/ETOH Mixture: Samples synthesized in W/ETOH (Figure 7-C) undergo multi-stage thermal decomposition, which differs from the other two mixtures.

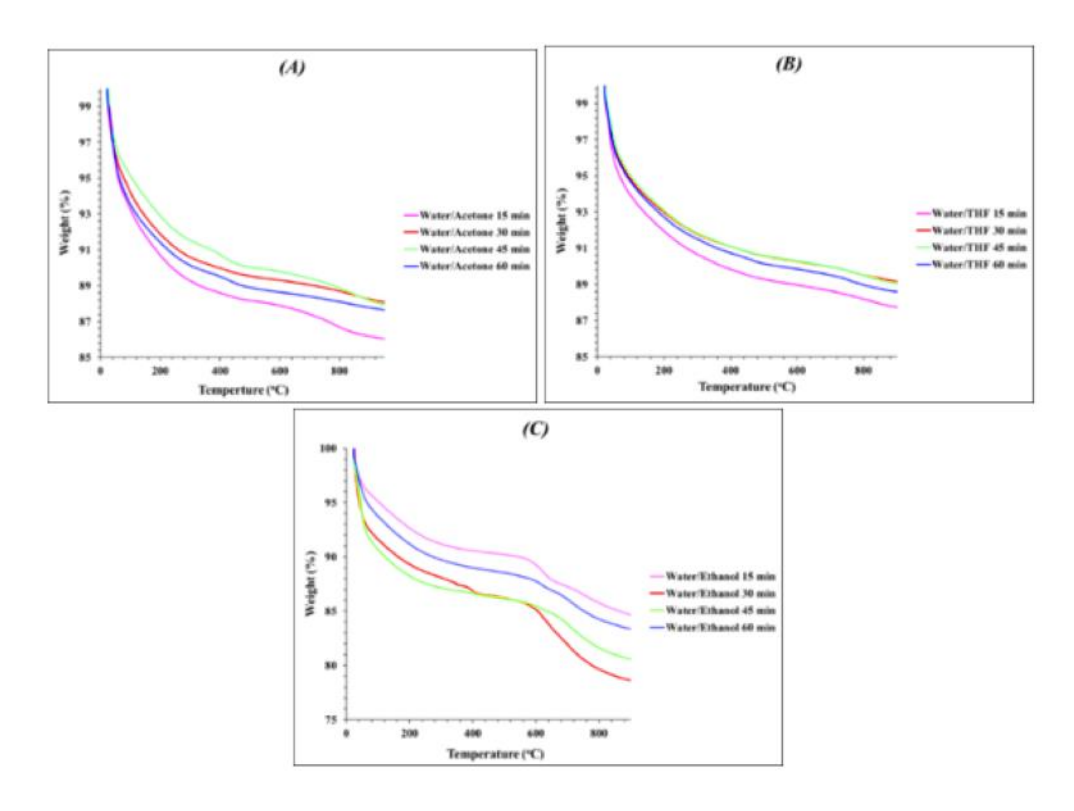


Figure 7: Thermograms of nHA synthesized in the mixtures: (A) W/ACET, (B) W/THF, (C) W/ETOH, at 15, 30, 45, and 60 minutes of UI.

Three thermal events are clearly visible. The most notable event occurs around 600

°C for the 15 and 60 minute curves. According to infrared and XRD characterizations, this behavior results from the formation of calcite formation as a secondary phase at these irradiation times. The small slope that appears 700 °C and 800 °C corresponds to the thermal decomposition of the calcium carbonate phase [68,69], as shown by the following chemical reaction: $CaCO_{3(s)} \rightarrow CaO_{(s)} + CO_{2(g)}$ (17)

Some literature reports that hydroxyapatite synthesized in W/THF and W/ACET exhibits the thermal behavior of stoichiometric hydroxyapatite [70,71]. This finding is consistent with the calcium surplus previously observed in the W/ETOH samples [72,73], and it also supports the formation of calcite. On the other hand, when the thermal behavior of the nHA synthesized in this study is compared with that of previous studies, it is evident that, the nHA obtained here showed remarkable thermal stability

[74]. It has been previously reported that hydroxyapatite only undergoes transformations leading to its decomposition at temperatures above the range between 1000 and 1300 °C. This promotes the formation of other biocompatible phosphate species, such as tetracalcium phosphate (TTCP) and tricalcium phosphate (β -TCP) [75].

Field Emission Scanning Electron Microscopy (FESEM) Study

Figure 8 shows the morphology of nHA, obtained by field emission scanning electron microscopy for the nHA obtained after 15 minutes of ultrasonic irradiation (UI), in the three solvent mixtures described above. Hidroxyapatite in W/ACET: This material consists of aggregates of spherical particles ranging in size from 60 to 70 nm. The arrangement is random, forming irregular structures (Figure 10-A). Hidroxyapatite in W/THF: The particles are spherical and aggregated, and smaller ranging from 50 to 60 nm in size. Its morphology resembles a "cauliflower" [76], with better dispersion than the W/ACET sample (Figure 8-B). Hidroxyapatite in W/ETOH: This mixture produced a very varied morphology. It included rods, spheres, and irregular particles, with a significantly smaller average size between 30 and 40 nm. Section 2 shows supplementary information about the histograms detailing the variability in particle size of the obtained hydroxyapatite. The FESEM also revealed for these samples a "plate or flake" morphology [77,78] (Figures 8-D and 8-E), in which particles are arranged in thin, flat, overlapping layers. This structure resembles to the mineral phase found in bone and collagen [79].

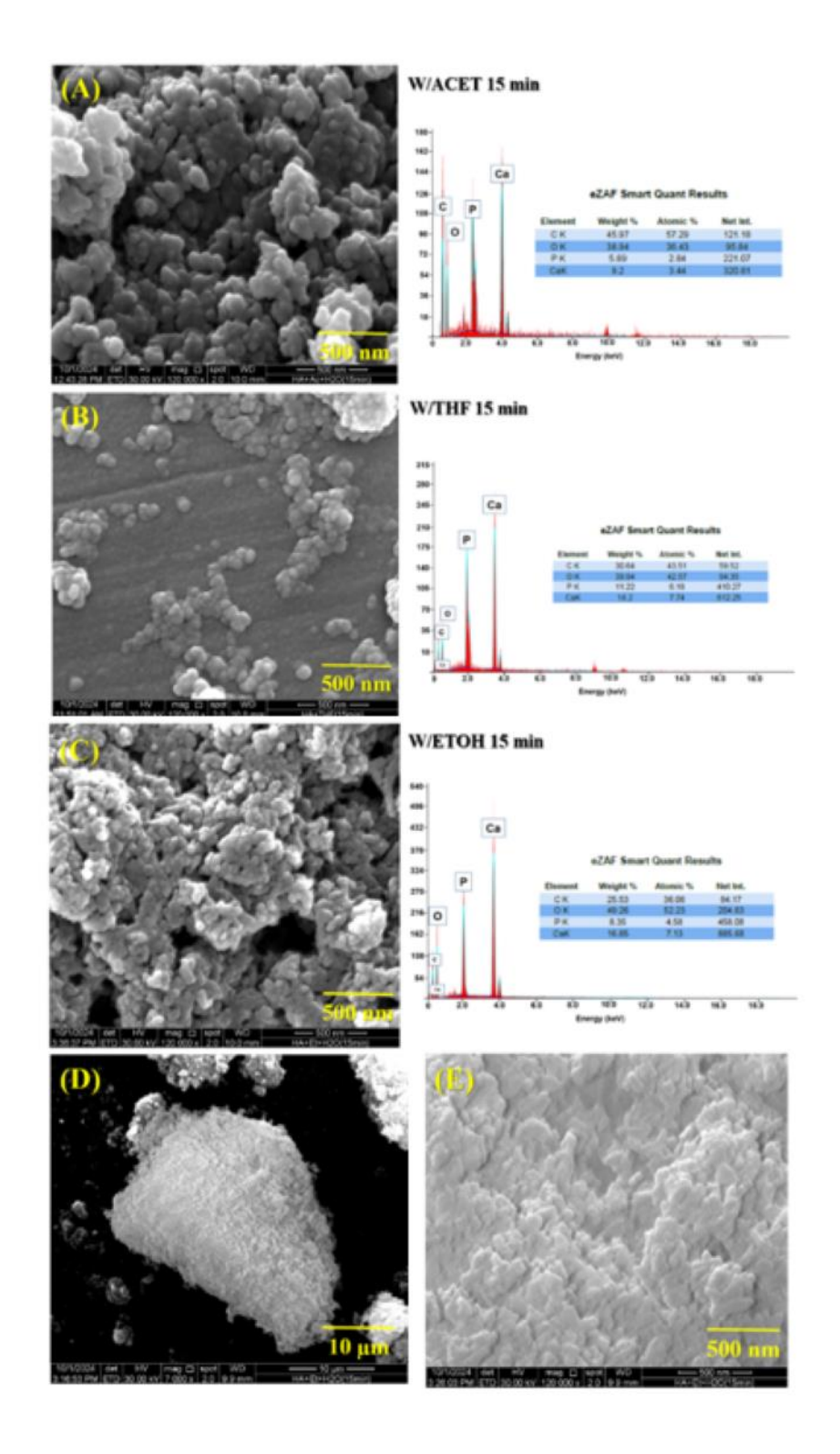


Figure 8: FESEM images of nHA synthesized after 15 minutes of ultrasonic irradiation: (A)

W/ACET, (B) W/THF, (D) and (E) W/ETOH mixtures.

The theory suggests that for W/ACET and W/THF mixtures, in the presence of aprotic solvents, that do not form hydrogen bonds, the electrostatic forces between hydroxyapatite-forming ions are robust. This results in faster nucleation, producing smaller particles with more regular morphologies. For the W/ETOH mixture, the formation of a nHA with multiple morphologies and reduced crystal size was favored [80]. Additionally, the co-precipitation of secondary phases, such as calcite was observed and definitely contributed to the morphological variations. The analysis also showed that the particle size decreased with increased exposure time to the high frequency ultrasound source in all three mixtures. This is especially relevant in terms of the yield of the synthesis reactions, as previously discussed. Details on the particle sizes obtained in each solvent mixture can be found in Section II of the supplementary information.

The Hemolytic effect of nanohydroxyapatite synthesized using high frequency ultrasound

Figure 9 shows the extent of the hemolytic effects of nHA samples synthesized at various UI time in W/THF solvent system. It is important to note here that these nHA samples were chosen as the standard ones for testing because they exhibited a fairly regular morphology, guarantee that no other crystalline phase formed during syntheses. Additionally, they demonstrated greater thermal stability according to TGA studies. As shown in Figure 9, all of the nHA produced at a concentration of 1.66 mg/mL induced very low levels of hemolysis, (less than 1% for the first hour and below 2% for the second hour of incubation), as determined by the percentage of hemolysis calculated using equation 20.

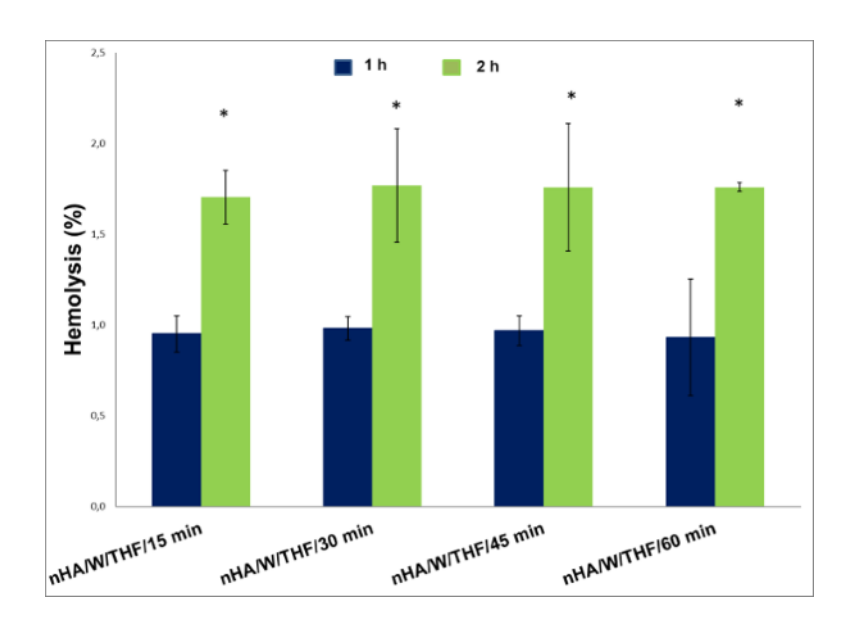


Figure 9: Effect of synthesized nHA in the water/THF mixture at 15, 30, 45, and 60 min of ultrasonic irradiation on the hemolysis of human blood. Values are means \pm S.D, n 3. Two-way ANOVA and Sidak's multiple comparisons test using GraphPad Prism 6.1 software were used. Differences between time points per each HA samples were considered statistically significant when the p-value < 0.05(*).

For hemolysis, there were no significant differences between the nHA samples. However, were significant differences between the times evaluated (1h and 2h) for each sample. These results indicate that the synthesized nHA tested may be considered as non-hemolytic according to the ASTM standard F756-00 [81], which defines three levels of material hemolytic potential: non-hemolytic (<2% hemolysis), slightly or mildly hemolytic (2-5% hemolysis), and highly hemolytic (>5% hemolysis). These hemolysis values are comparable to those of other hydroxyapatites. For example, Barbosa et al [82] using washed mouse red blood cells reported < 2% hemolysis for hydroxyapatite tested up to 1 mg/mL for 1 hour; and Radha et al [83] using washed human red blood cells reported < 2% of hemolysis for nHA tested up to

40 mg/mL for 1 hour and less than 4% hemolysis for nHA tested up to 100 mg/mL for 1 hour.

As the hemolytic activity is directly proportional to the diameter of the nanoparticles [84] the observed behavior could be related to the fact that the nHA obtained in the W/THF mixture exhibited very small particle sizes.

At this point, it is important to highlight that the hemolytic response can be altered by the presence of any additive or by remnants of the substances used as precursors of the biomaterial, or surface roughness. These factors can cause substantial changes in blood behavior, leading to erroneous results [85]. In this sense, the sonochemical synthesis used to obtain nHA in this research, is simple and chemically clean, aligning with the principles of green chemistry.

Figure 10 shows optical microscopy images of red blood cells from the bottom of the remaining fraction from which the supernatant was taken to test for hemolytic activity. As expected, the negative (A) and positive (B) controls show the presence and absence of red blood cells in saline solution and distilled water, respectively.

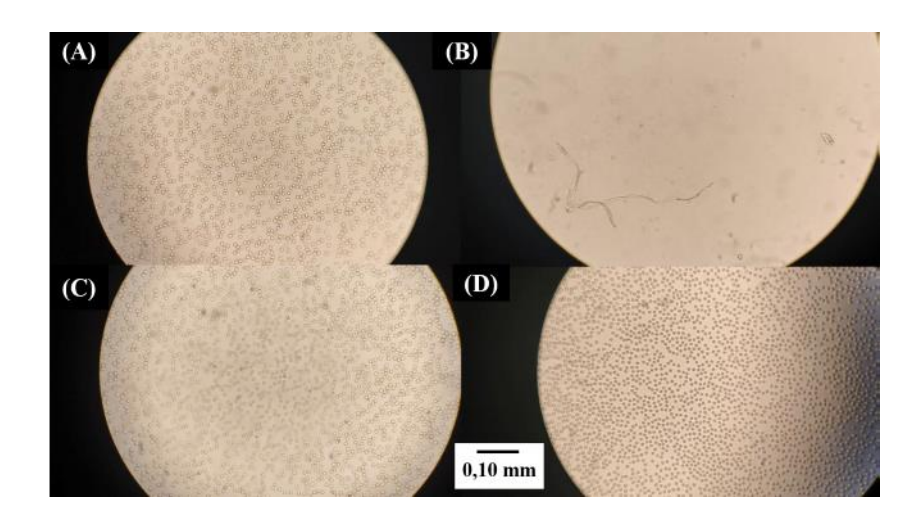


Figure 10: Optical microscopy images 40X of red blood cells obtained after incubation at 37 °C for 1 hour with: (A) 0.9% saline solution (negative hemolysis control), (B) distilled water

(positive hemolysis control), (C) and (D) nHA W/THF obtained at 15 and 60 minutes of UI respectively.

In (C) a high percentage of red blood cells are evident, though not quantified. These cells are preserved, characterized by rounded cell contours and a clear interior, similar to those observed in (A). However, few dark blood cells and dark external areas are also observed. In (D), slightly smaller red blood cells with a darker interior than those observed in the control (A) are evident, though they have the same rounded cell contours. Further studies are needed to determine the metabolic or osmotic nature of the darkness induced by nHA in red blood cells.

A slight increase in the number of red blood cells was observed when the negative was compared to the HA samples synthesized after 15 and 60 minutes of irradiation, respectively (Figures 10-C and 10-D). The greatest effect was observed in Figure 10-D. On the other hand, in Figures 10-C and 10-D, show that there are no structural modifications in erythrocytes which maintain their spherical morphology.

When assessing the hemotoxicity of a biomaterial, platelet aggregation must also be studied. This process is crucial for preventing many circulation-related diseases and pathologies, such as strokes and heart attacks, due to its great complexity [86].

In vitro evaluation of biomaterial hemocompatibility requires studying protein adsorption, blood cell attachment (red and white cells and also platelets), and thrombus and fibrin network generation (Werber et al) [87]. Among them, interaction of the biomaterial with platelets must be studied, since they participate in the first events that lead to the formation of blood clots, which are associated with the development of strokes and heart attacks [88]. Therefore, to evaluate the effect of HA synthesized in W/THF on platelets, in vitro platelet aggregation tests were performed.

Table 4: Effect of nHA-W/THF (15 and 60 minutes) on human platelet aggregation induced by ADP

Sample	Platelet Aggregation				
Sample	MaxA	SLP	AUC		
Saline	93.67 ± 1.44	121 ± 18.38	557.72 ± 18.76		
solution	(100 %)	(100 %)	(100 %)		
nHA-15	97.17 ± 2.31	126.5 ± 11.30	578.58 ± 20.83		
	(103.74 %)	(104.55 %)	(103.74 %)		
nHA-60	93.67 ± 2.08	108.67 ± 10.52	550.38 ± 19.55		
	(100.1 %)	(89.81 %)	(98.69 %)		

Human platelet aggregation induced by ADP (10 uM) was measured by maximal aggregation (MaxA), slope of the first phase of platelet aggregation (SLP) and area under the curve (AUC), in the absence (control using saline solution) or in the presence of samples pre-incubated at 37 oC for 15 minutes. Values are means ± S.D, n 3. Samples: nHA-15, nHA-60: hydroxyapatite synthesized at 15 and 60 min of ultrasonic irradiation, respectively. One-way ANOVA and Bonferroni post hot test using GraphPad Prism 6.1 software were used. Differences between the responses are not considered statistically significant.

Table 4 shows that W/THF nHA-15 and nHA-60 at (~0.11 mg/mL) do not affect the aggregation of human platelets. These compounds do not affect the magnitude of the maximum response (MaxA), the speed of the first phase of aggregation (SLP) or the integral measurement of the entire aggregation process (AUC). Small variations (<10%) were observed, but they were not significant with respect to the control condition. The inability of synthesized nHA to alter the natural process of platelet aggregation is very favorable and beneficial for potential biomedical applications and leads to its consideration as a platelet-compatible biomaterial.

This result is important because platelets undergo a biological activation in the presence of foreign agents in the body. This activation causes the platelets to change their shape, adhere to each other to form clumps and release molecules and substances that regulate the immune response and blood coagulation [89]. This progressive union of platelets and coagulation factors can have negative effects on a

patient's physical integrity such as the formation of thrombi which could lead to a stroke [89].

Based on these results it can be concluded that nHA synthesized using ultrasonic irradiation as an energy source can be considered as hemocompatible materials, as defined by ISO 10993-4 [90], since they present a very low hemolytic risk and does not interfere with the initial phase of hemostasis (platelet activation).

Antibiofilm properties of hydroxyapatite variants synthesized using UI

This research evaluated the capability of nHA variants synthesized using ultrasonic irradiation to reduce the risk of *P. aeruginosa* ATCC 10145 attachment or biofilm formation on surfaces tested by the crystal violet staining. This method allows for biomass quantification, which is the total mass of bacterial cell growth in a given sample. It is also a key indicator of bacterial abundance and biofilm formation. Our results showed a statistically significant reduction (p<0.05) in biomass for samples exposed to nHA/W/ETOH/15 min and nHA/W/ETOH/60 min compared to the commercial hydroxyapatite (CHA), with respective decreases of 60.7% and 30.3% (Fig. 11).

Additionally, SEM analysis demonstrates few rod cells (1-2 µm) adhered to the test surfaces in the nHA/W/ETOH/15 sample (Fig. 12 A-B). This sample was selected because it showed the highest biomass reduction. In contrast, the CHA exhibited higher cellular aggregation or microcolonies embedded in exopolysaccharides with dispersed crystalline-like structures (Fig. 12 C-D). This phenomenon has been previously reported in the biofilms of other bacterial species such as Proteus mirabilis [91,92]. Other highly organized structures besides crystalline-like formations, such as mushrooms, have been described in *P. aeruginosa* these structures are believed to

allow nutrients to pass from the upper to deeper levels of biofilms [93]. Finally, control surfaces exhibited no bacterial adhesion (data not shown).

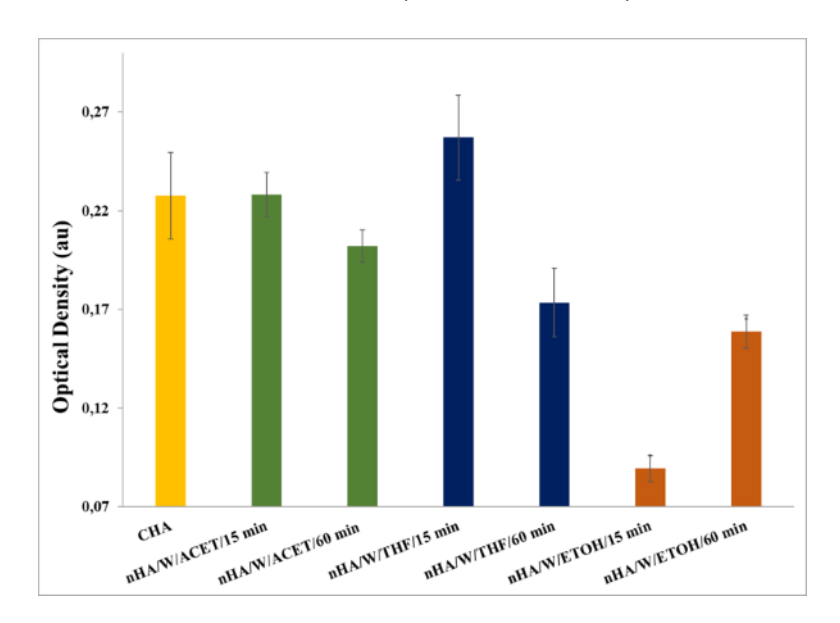


Figure 11: Antibiofilm potential of nHA synthesized with W/ACET, W/THF, W/ETOH mixtures at 15 and 60 min of UI against *P. aeruginosa* ATCC 10145.

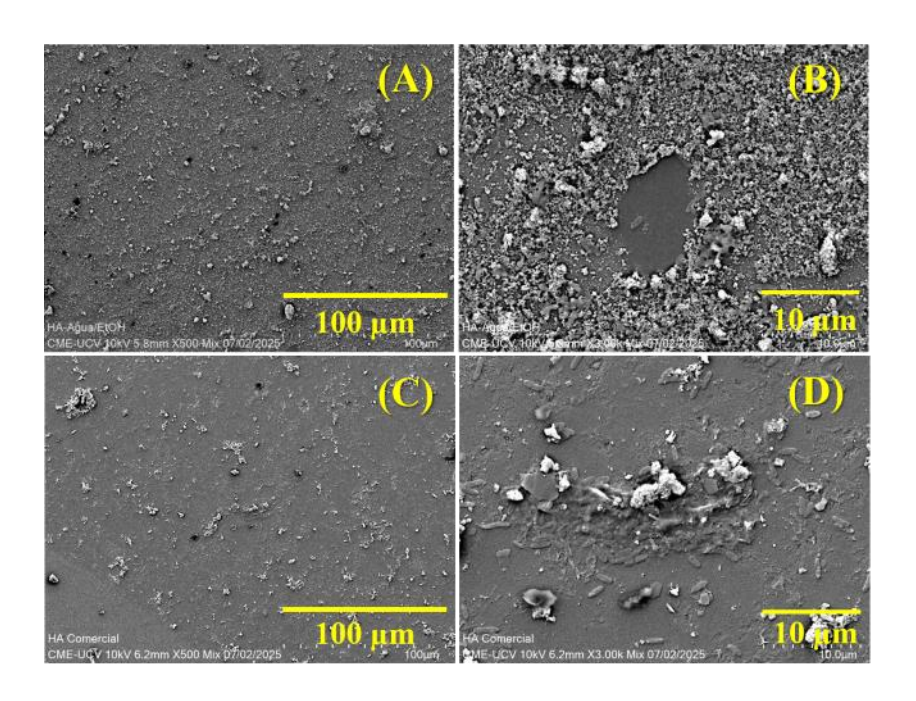


Figure 12: Representative SEM images of *P. aeruginosa* colonization in test surfaces of nHA variants synthesized by UI. (A-B) nHA/W/ETOH/15 min at 100 and 10 μm, respectively; (C-D) Commercial hydroxyapatite at 100 and 10 μm, respectively.

Overall, this work evidences the potential use of nHA variants synthesized with UI to control P. aeruginosa biofilm-related infections on indwelling medical devices, as well as contributes to the current knowledge of chemically friendly nHA synthesis techniques, with biomedical and antibiofilm applications. Further research is needed to the better understand the key mechanisms involved in the antibiofilm activity of these composites in order to advance in the prevention and control measures of bacterial colonization on hydroxyapatite prostheses and minimize their public health risks.

CONCLUSIONS

The ultrasonic-assisted synthesis of highly biocompatible nHA was successfully carried out, with a yield percentage exceeding 80%. Under all the reaction conditions employed and based on the results obtained by FTIR and XRD, the formation of a carbonated hydroxyapatite with a hexagonal crystalline structure and high thermal stability was confirmed. FESEM studies revealed that the microstructure of the nHA was composed was composed of particles on the nanometric scale. The ultrasonic irradiation applied and the physicochemical characteristics of the solvent mixtures used as the reaction medium had significantly influenced on the morphology of the nHA. Hemocompatibility studies showed that the HA obtained with high-frequency ultrasound was very low hemotoxic and it did not affect platelet aggregation. This endows the material with crucial properties for the hemostasis process. Microbiological assays showed a significant reduction in the biomass production of P. aeruginosa for the nHA synthesized in the W/ETOH mixture, as well as lower bacterial colonization, formation of cellular aggregates, or specialized structures when treated with this material, compared to a commercially sourced HA. This suggests potential antibiofilm properties. Consistent with these results, ultrasonic irradiation promotes the formation of a high-purity hydroxyapatite, with improved general properties, and offers new perspectives for obtaining this important bioceramic, outlining its potential use in biomedical applications.

EXPERIMENTAL

Synthesis of nanohydroxyapatite (nHA)

Ca (OH)₂ (MW: 74.10 g/mol, 96% purity) and (NH₄)₂HPO₄ (MW: 132.05 g/mol, 99% purity) were used as the initial reactants to obtain nHA. The masses of these precursors were chosen to achieve a Ca/P ratio of 1.67 [94], based on the stoichiometry of the chemical reaction indicated by equation number 18.

10 Ca(OH)₂ + (NH₄)₂HPO₄
$$\rightarrow$$
 Ca₁₀(PO₄)₆(OH)₂ + 12NH₄OH + 6H₂O (18)

Both precursors were added to a beaker together with 40 mL of a solvent mixture: W/ACET (Acetone by Riedel-de Haën, B.P: 66 oC, MW: 72.11 g/mol,), W/THF (THF by Riedel-de Haën, B.P: 56 °C, MW: 58.08 g/mol), W/ETOH (Ethanol by Riedel-de Haën, B.P: 78°C, 46.06 g/mol); in a 1:1 ratio. The solids (calcium hydroxide and ammonium acid phosphate) were dispersed in the solvents by magnetic stirring for 2-5 minutes. The resulting suspensions were exposed to ultrasonic irradiation (UI) for controlled periods of time (15, 30, 45, and 60 min) using a Fisher 150W Ultrasonic Generator, operating at a nominal frequency of 20 kHz. After each reaction, the resulting solid was washed several times with abundant preheated distilled water (50-80°C), using a Thermo Scientific Sorvall Legend T+ centrifuge at 3700 rpm, in order to remove the reaction by-products. Then, the nHA obtained was dried in a Fischer Isotemp Oven 350 stove at a temperature of 40 °C and atmospheric pressure it reached a constant weight. The dried samples were crushed in an agate mortar to achieve a fine powder consistency. All syntheses were carried out in duplicate. Table 5 summarizes the general reaction conditions.

Table 5: Matrix of synthesis conditions to obtain hydroxyapatite

Experiment	Solvent mixture	Irradiation time (min)	
1		15	
2	W/ACET	30	
3	VV/ACE I	45	
4		60	
5		15	
6	\A//TIIF	30	
7	W/THF	45	
8		60	
9		15	
10	W/ETOLI	30	
11	W/ETOH	45	
12		60	

Physicochemical and structural characterization of hydroxyapatite Infrared Spectroscopy (FTIR)

This technique enabled the identification of the characteristic absorption bands of nHA, prepared in the different solvent mixtures as shown in Table 5. To accomplish this, mixtures of nHA and KBr were prepared at a ratio of 200 mg KBr/0.8 mg of the sample to be analyzed. They were pulverized and thoroughly mixed in an agate mortar. Then, they were subjected to a pressure of 30 tons using a press to obtain compact pellets. Finally, the pellets were analyzed using a Perkin Elmer Spectrum 100 spectrometer in the wavenumber range from 4000 to 450 cm⁻¹.

X-Ray Diffraction

X-ray diffraction (XRD) studies were performed to identify the crystalline structure of nHA. The tests were performed using a FRINGE Benchtop X-Ray diffractometer from LanScientific, operating at 30kV and 16 mA, with the kα line of a copper lamp to study the solids.

Thermogravimetric analysis (TGA)

TGA studies were conducted to evaluate the thermal stability of hydroxyapatite. These tests were performed using TA Instrument SDT Q600 V7.0 Build 84 equipment. The different samples were analyzed at temperatures ranging from 25°C to 1000°C, in an air atmosphere at a heating rate of 10°C/min.

Field emission scanning electron microscopy (FESEM) and energy dispersive X-ray spectroscopy (EDX)

To reveal the morphology of the synthesized hydroxyapatite, an INSPECT-F50 field emission scanning electron microscope, operating at 30 kV was used. The samples were prepared using two methods: in the first, called the dry method, the powder was uniformly dispersed directly onto a carbon tape. In the second, called the wet method, the samples were placed in an ethanol-water solution and stirred in an ultrasonic bath until a suspension was formed. Then, a drop was placed on an aluminum sample holder and dried in an oven at 40 °C. Finally, all samples were coated with gold.

Determination of Hydroxyapatite Synthesis Yield

The efficiency of the synthesis process with ultrasonic irradiation was determined based on the stoichiometry of the reaction (Equation 18) to calculate yield, using the relationship in Equation 19:

Yield (%) =
$$\frac{moles\ of\ nHA\ obtained}{moles\ of\ nHA\ theoretical}\ x\ 100$$
 (19)

(Ammonium phosphate being the limiting reagent)

Evaluation of the biological effects of hydroxyapatite samples

To evaluate the hemocompatibility of hydroxyapatite samples hemolysis assay and *in vitro* human platelet aggregation were performed. Six volunteers gave their informed consent approved by the Human Bioethical Committee of the Venezuelan Institute of Scientific Research (DIR-0997/1569/2016).

Hemocompatibility assay

This analysis was performed only on nHA samples, which were synthesized in W/THF, at all UI times (15, 30, 45, and 60 min). The protocol used was modified from Pal et al. [36]. The collected blood was anticoagulated with 3.2% sodium citrate in a 9:1 blood-to-citrate ratio. One (1) mg of each nHA sample was dispersed in 300 μ L of the anticoagulated blood and 300 μ L of saline solution (0.9% sodium chloride). The samples were then mixed gently and incubated at 37 °C for 1 and 2 hours, under constant agitation (1000 rpm). For hemolysis controls, 300 μ L of anticoagulated blood was diluted with either 300 μ L of saline (negative control) or 300 μ L of distilled water (positive control), and incubated in the same manner as the nHA samples. After the incubation period (1 and 2 hours), 20 μ L of each sample nHA and control were taken and diluted with 1000 μ L of saline solution, then it was centrifuged at 3000 rpm for 8 min. Finally, the absorbance of each supernatant (250 μ L) was measured at a wavelength of 545 nm using a BioTek Power Wave XS2 spectrophotometer. The absorbance results obtained were processed to determine the percentage of hemolysis, using the expression in equation 20.

Hemolysis percentage (%) =
$$\frac{A_{sample} - A_{negative \ control}}{A_{positive \ control} - A_{negative \ control}} * 100$$
 (20)

A sample: absorbance of the sample under study

A negative control: absorbance of the negative control (saline solution)

A positive control: absorbance of the positive control (distilled water)

In Vitro Human Platelet Aggregation

Human platelets were obtained from blood of healthy volunteers who had not taken

any drugs the previous two weeks. Platelet rich plasma (PRP) was prepared and used

in platelet aggregation assays as previously described by Estrada et al □37□. Briefly,

10 µL of the nHA under study (4 mg/mL, suspended in saline solution) were added to

350 µL of PRP for 15 min at 37°C prior to the stimulation of platelet aggregation

(Chrono-Log model 700) by Adenosine diphosphate (ADP, Sigma Aldrich USA) (10

μM), under constant agitation (1000 rpm). Control ADP-platelet aggregation was

performed using 10 µL of saline solution instead of the nHA samples. Three replicates

of each condition were performed. Maximal aggregation (MaxA), slope of the first

phase of platelet aggregation (SLP) and area under the curve (AUC), were calculated

using the software application Aggrolink 8 (Chrono-Log Corporation, USA).

Study of antibiofilm properties

In vitro biofilm assays

The P. aeruginosa ATCC 10145 reference strain was cultured in nutrient broth and

cetrimide agar (Difco, Detroit, MI, USA) at 37 °C for 24-48 hours then stored at -80 °C.

To evaluate the antibiofilm effectiveness of nHA synthesized with UI against this

pathogen, the bacterial cells were grown in Luria Bertani (LB) broth at 37°C until the

early logarithmic phase (0.2 optical density, OD), cultured in 24 well microplates

containing glass surfaces (1 cm²) as sample supports and exposed under sterile

conditions to a commercially available medical-grade HA as reference material as well

35

as to nHA variants obtained with three solvent mixtures (W/ACET, W/THF and W/ETOH), which were used for this microbiological study.

Previously, dispersions of all nHA samples were prepared at a concentration of 1 mg/mL. This was done by adding 5 mg of nHA to 5 mL of a 70%-30% ethanol-water solution and digesting the mixture in an ultrasonic bath (42 kHz; 10 min) until it was homogeneous. When homogenization was achieved, 100 µL of the nHA suspensions were deposited onto glass surfaces and sterilized by irradiating them with a cobalt-60 gamma ray source (36 kGy; JS-9500 irradiator, MDS Nordion, Canada) at the PEGAMMA Plant of IVIC. Wells containing surfaces and nHA variants without inoculum were included as negative controls. Wells containing surfaces and inoculum without nHA were considered as control of biofilm growth. After each incubation time, all samples were removed and rinsed three times with phosphate buffered saline (PBS, 0.1 M, pH 7.4). Then, they were transferred to wells of a microtiter dish. To quantify the biomass of the biofilms, the cells attached to the surfaces of the five replicates were stained with a 0.5% solution of crystal violet (CV), incubated at room temperature for 15 min and then resuspended in 95% ethanol. The absorbance at 600 nm of the resuspended CV was determined and normalized to the OD 600 nm of the corresponding grows cells density. The biomass was expressed as ng/mL [97]. Statistical comparisons in the biomass production among the tested surfaces were obtained using PAST software (v. 3.14) and the nonparametric Kruskal-Wallis test for two independent samples. P values < 0.05 were considered significant.

To observe the morphology of the biofilms using SEM, duplicate samples were washed twice with sterile distilled water and fixed with 2.5% glutaraldehyde at 4 °C Then, the samples were washed with cold distilled water washings, dehydrated with 50% ethanol for 10 min, dried at 40 °C and coated with gold (glued to the holders using die-cut carbon conductive adhesive discs; SPI Supplies/Structure Probe, Inc., West Chester,

PA, USA). Three to five different measurement positions on the surface of each sample were chosen randomly to obtain representative images over biofilm formation using a Hitachi TM 4000 (Hitachi, Tokyo, Japan) operated at a variable pressure (6-8 mm Hg) and 15 kV of acceleration voltage.

Statistical analysis

Values are expressed as the mean and standard deviation (SD) and n represents the number of experiments performed. Statistical analysis was performed applying Oneway ANOVA and Bonferroni post hoc tests or two-way ANOVA and Sidak's multiple comparisons test, as indicated, using GraphPad Prism 6.1 software. Differences between responses were considered statistically significant when the P-value < 0.05(*).

Supporting Information

Supporting Information File 1:

Section I-General assignment of infrared bands of Nanohydroxyapatite

Supporting Information File 2:

Section II-Histograms with hydroxyapatite particle sizes

Acknowledgements

The authors of this work would like to thank the following people and institutions for their contributions to this research: Bachelor Rosamar Lugo (Research Associate Professional), Bachelor Andreina Bendayán (Research Associate Professional), Higher University Technician Jessica Rodríguez (Research Associate Technician), Bionanotechnology Laboratory, Center for Materials Engineering and Nanotechnology, IVIC). To the personnel of the Pegamma plant, Physics Center, IVIC. To the personnel

of the Microscopy Center "Dr. Mitsuo Ogura", Faculty of Sciences, UCV. To the personnel of the Electron Microscopy Unit of the "Dr. Gabriel Chuchani" Chemistry Center, IVIC. To the personnel of the Laboratory of Diffraction and X-Ray Fluorescence, Department of Geology, Faculty of Engineering, UCV.

Funding

The reagents and equipment used for the synthesis and characterization of the nanohydroxyapatite samples were provided by the IVIC Materials Engineering and Nanotechnology Center.

References

- 1. Todros, S.; Todesco, M.; Bagno, A. Processes. 2021, 9, 1949.
- 2. Chen, R. K.; Wensman, J.; Shih, A. Addit. Manuf. 2016, 12, 77-89.
- 3. Barrios-Muriel, J.; Romero-Sánchez*, F.; Alonso-Sánchez, F. J.; and Rodríguez Salgado, D. Materials. 2020, 13, 295.
- 4. Powell*, S. K.; Cruz, R. L. J.; Ross, M. T.; and Woodruff, M. A. Adv. Mater. 2020, 32, 2001122.
- 5. Perera, A. S.; Coppens, M. O. Phil. Trans. R. Soc. A. 2019, 377, 20180268.
- 6. Eichert, D.; Sfihi, H.; Combes, C.; Rey, C. Key Eng. Mater. 2004, 254, 927-930.
- 7. Rhee, S-H.; Lee, J. D.; Tanaka, J. J. Am. Ceram. Soc. 2000, 83, 2890-2892.
- 8. Osuchukwu, O. A.; Salihi, A.; Abdullahi, I.; Abdulkareem, B.; & Nwannenna, C. S. SN Appl. Sci. 2021, 3, 1-23.
- 9. DileepKumar, V. G.; Sridhar, M. S.; Aramwit, P.; Krut'ko, V. K.; Musskaya, O. N.; Glazov, I. E.; Reddy, N. A. J. Biomater. Sci. Polym. Ed. 2022, 33, 229-261.
- 10. Agbeboh, N. I.; Oladele, I. O.; Daramola, O. O.; Adediran, A. A.; Olasukanmi, O. O.; & Tanimola, M. O. 2020, 6, e03765.

- 11. Kolanthai, E.; Ganesan, K.; Epple, M.; & Kalkura, S. N. Mater. Today Commun. 2016, 8, 31-40.
- 12. Sun, W.; Fan*, J.; Wang, S.; Kang, Y.; Du, J.; Peng, X. ACS Appl. Mater. Interfaces. 2018, 10, 7832-7840.
- 13. Arcos*, D.; Vallet-Regí, M. J. Mater. Chem. B. 2020, 4, 1781-1800.
- 14. Ebrahimi, S.; Stephen Sipaut@ Mohd Nasri, C.; Bin Arshad, S. E. PLoS One. 2021, 16, e0251009.
- 15. Wu, S. C.; Hsu, H. C.; Wang, H. F.; Liou, S. P.; Ho, W. F. Molecules. 2023, 28 4926.
- 16. Mason, T. J.; Vinatoru, M. Sonochemistry: fundamentals and evolution, Walter de Gruyter GmbH & Co KG, 2023.
- 17. Li, Z.; Dong, J.; Zhang, H.; Zhang, Y.; Wang, H.; Cui, X.; and Wang, Z. Nanoscale Adv. 2021, 3. 40.
- 18. Xu, H.; Zeiger, B. W.; and Suslick*, K. S. Chem. Soc. Rev. 2013, 42, 2555.
- 19. Deng, S. T.; Yu, H.; Liu, D.; Bi, Yg. Appl. Phys. A. 2017, 123, 642.
- 20. Stanislavov, A. S.; Sukhodub, L. F.; Sukhodub, L. B.; Kuznetsov, V. N.; Bychkov, K. L.; Kravchenko, M. I. Ultrason. Sonochem. 2018, 42, 84-96.
- 21. Mostovshchikov, A.V.; Grebnev, M. E.; Rudmin, M. A.; Nazarenko*, O. B.; Derina, K.V.; Galtseva, O.V. Eurasian. phys. tech. j. 2024, 21, 3.
- 22. Shah Rizal Kasim, I. E.; Baba Ismail, Y. M.; and Mohd Noor, A-F. Ceram. Int. 2018, 44, 13082-13089.
- 23. González, G.; Costa-Vera, C.; Borrero, L. J.; Soto, D.; Lozada, L.; Chango, J. I.; Díaz, J. C.; Lascano, L. J. Lumin. 2018, 195, 385-395.
- 24. Tozar, A.; and Karahan, I. H. Bioinspir. Biomim. Nan. 2018, 7, 149-158.
- 25. Abdussalam-Mohammed, W.; Ali, A. Q.; Errayes, A. O. Chem. Methodol. 2020, 4, 408-423.
- 26. Sheldon, R. A. ACS Sustain. Chem. Eng. 2018, 6, 32-48.
- 27. AbouAitah, K.; Bil, M.; Pietrzykowska, E.; Szałaj, U.; Fudala, D.; Woźniak, B.; ... & Lojkowski, W. Nanomater. 2021, 11, 1690.

- 28. Lamkhao, S.; Phaya, M.; Jansakun, C.; Chandet, N.; Thongkorn, K.; Rujijanagul, G.; Bangrak, P.; Randorn, C. Sci. Rep. 2019, 9, 4015.
- 29. Puvvada, N.; Panigrahi, P. K.; & Pathak, A. Nanoscale. 2010, 2, 2631-2638.
- 30. Zakharova, O. V.; Vasyukova, I. A.; Gusev, A. A.; Chuprunov, K. O.; Yudin, A. G.; & Kuznetsov, D. V. Nanotechnol Russ. 2019, 14, 405-409.
- 31. Klockgether, J. & Burkhard, T. F1000Res. 2017, 1261.
- 32. Costerton, J. W. Int. J. Antimicrob. Agents. 1999, 11, 217-239.
- 33. Donlan, R. M. Clin. Infect. Dis. 2001, 33, 1387-1392.
- 34. Franklin, M. J.; Nivens, D. E.; Weadge, J. T.; & Howell, P. L. Front. Microbiol. 2011, 2, 167.
- 35. Youness, R. A.; Taha, M. A.; Elhaes, H.; & Ibrahim, M. Mater. Chem. Phys. 2017, 190, 209-218.
- 36. Anjaneyulu, U.; Priyadarshini, B.; Stango, S. A.; Chellappa, M.; Geetha, M.; & Vijayalakshmi, U. Mater. Technol. 2017, 32, 800-814.
- 37. Xue, C.; Chen, Y.; Huang, Y.; & Zhu, P. Nanoscale Res Lett. 2015, 10, 316.
- 38. Cacciotti, I. Cationic and anionic substitutions in hydroxyapatite. Handbook of bioceramics and biocomposites. Springer, Cham, 2015. 1-68.
- 39. Porter, A.; Patel, N.; Brooks, R.; Best, S.; Rushton, N.; & Bonfield, W. J. Mater. Sci. Mater. Med. 2005, 16, 899-907.
- 40. Ribeiro, C. C.; Gibson, I.; & Barbosa, M. A. Biomaterials. 2006, 27, 1749-1761.
- 41. Ma, J.; Wang, Y.; Zhou, L.; & Zhang, S. Mater. Sci. Eng. C. 2013, 33, 440-445.
- 42. Siddiqi, S. A.; & Azhar, U. Carbonate substituted hydroxyapatite. In Handbook of ionic substituted hydroxyapatites. Woodhead Publishing, 2020; p 149-173.
- 43. Thang, L. H.; Bang, L. T.; Long, B. D.; Son, N. A; & Ramesh, S. J. Mater. Eng. Perform. 2023, 32, 1006-1016.
- 44. Bulina, N. V., Makarova, S. V., Baev, S. G., Matvienko, A. A., Gerasimov, K. B., Logutenko, O. A., & Bystrov, V. S. Minerals. 2021, 11, 1310.
- 45. Zou, Z.; Lin, K.; Chen, L.; & Chang, J. Ultrason. Sonochem. 2012, 19 1174-1179.

- 46. Yoder, C.; Pasteris, J.; Worcester, K.; Schermerhorn, D.; Sternlieb, M.; Goldenberg, J.; & Wilt, Z. Minerals, 2012, 2, 100-117.
- 47. Fiume, E.; Magnaterra, G.; Rahdar, A.; Verné, E.; Baino, F. Ceram. 2021, 4, 542-563.
- 48. Cox, S. C.; Walton, R. I.; & Mallick, K. K. Bioinspir. Biomim. Nan. 2015, 4, 37-47.
- 49. Perea, G. N. R.; Silva, M. B.; Freitas, B. X.; dos Santos, É. M. B.; Lopes, L. C. R.; Vitorazi, L.; & dos Santos, C. Res. Soc. Dev. 2020, 9, e30791210996.
- 50. Sossa, P. A. F.; Giraldo, B. S.; Garcia, B. C. G.; Parra, E. R.; & Arango, P. J. A. Mater. 2018, 23, e12217.
- 51. Anwar, A.; Asghar, M. N.; Kanwal, Q.; Kazmi, M.; & Sadiqa, A. J. Mol. Struct. 2016, 1117, 283-286.
- 52. Marković, S.; Veselinović, L.; Lukić, M. J.; Karanović, L.; Braćko, I.; Ignjatović, N. and Uskokoví, D. Biomed. Mater. 2011, 6, 045005.
- 53. Karunakaran, G.; Kumar, G. S.; Cho, E.-B.; Sunwoo, Y.; Kolesnikov, E. and Kuznetsov, D. Ceram. Int. 2019, 45, 970-977.
- 54. Mondal, S.; Hoang, G.; Manivasagan, P.; Moorthy, M. S.; Kim, H. H.; Phan, T. T. V.; & Oh, J. Mater. Chem. Phys. 2019, 228, 344-356.
- 55. Sari, M.; Ashilawati, A.; Khoir, L.; Wahyuningsih, R.; & Yusuf, Y. J. Biomim. Biomater. Biomed. Eng. 2023, 62, 1-7.
- 56. Utara, S.; & Klinkaewnarong, J. Micro nano lett. 2015, 10, 1-4.
- 57. Barbosa, M. C.; Messmer, N. R.; Brazil, T. R.; Marciano, F. R.; Lobo, A. O. Mater. Sci. Eng. C. 2013, 33, 2620-2625.
- 58. Jebri, S.; Khattech, I.; & Jemal, M. J. Chem. Thermodyn. 2017, 106, 84-94.
- 59. Nan, Z. D.; Z. Shi, Y.; Qin, M.; Hou, W. G.; & Tan, Z. C. Chin. J. Chem. 2007, 25, 592-595.
- 60. Kitamura*, M.; Konnob, H.; Yasuia, A.; Masuoka, H. J. Cryst. Growth. 2002, 236, 323-332.
- 61. Rumble, J.R.; CRC Handbook of Chemistry and Physics. 97th ed. Boca Raton: CRC Press, 2017.

- 62. Mizukoshi, Y.; Nakamura, H.; Bandow, H.; Maeda, Y.; & Nagata, Y. Ultrason. Sonochem. 1999, 6, 203-209.
- 63. Bell, L. C.; Mika, H. & Kruger, B. J. Arch. Oral Biol. 1978, 23, 329-336.
- 64. Mohsen-Nia, M.; Amiri, H. & Jazi, J. Solut. Chem. 2010, 39, 701-708.
- 65. Nazeer, MA.; Yilgor, E.; Yagci, MB.; Unal, U.; Yilgor, I. R. Soc. open sci. 2017, 4, 171098.
- 66. Sofronia, A. M.; Baies, R.; Anghel, E. M.; Marinescu, C. A.; & Tanasescu, S. Mater. Sci. Eng. C. 2014, 43, 153-163.
- 67. Liu,Q.; Matinlinna, J. P.; Chen, Z.; Ning, C.; Ni, G.; Pan, H. & Darvell, B. W. Ceram. Int. 2015, 41, 6149-6157.
- 68. Al Omari, M. M. H.; I. Rashid, S.; Qinna, N. A.; Jaber, A. M. & Badwan, A. A. 2016, 41, 31-132.
- 69. Barinov, S. M.; Rau, J. V.; Cesaro, S. N.; Ďurišin, J.; Fadeeva, I. V.; Ferro, D. & Trionfetti, G. J. Mater. Sci.: Mater. Med. 2006, 17, 597-604.
- 70. Rajkumar, M.; Sundaram, N. M. & Rajendran, V. Dig. J. Nanomater. Biostruct. 2011, 6, 169-179.
- 71. Chaikina, M. V.; Bulina, N. V.; Vinokurova, O. B.; Gerasimov, K. B.; Prosanov, I. Y.; Kompankov, N. B.; Lapina, O. B.; Papulovskiy, E. S.; Ishchenko, A. V.; Makarova, S. V. 2022, 5, 404-422.
- 72. Zhang, H. & Darvell, B. W. Acta Biomater. 2011, 7, 2960-2968.
- 73. Giardina, M. A.; Fanovich*, M. A. Ceram. Int. 2010, 36, 1961-1969.
- 74. Prakash, V. C. A.; Venda, I.; Thamizharasi, V. & Sathya, E. Mater. Chem. Phys. 2021, 259, 124097.
- 75. Ou, S. F.; Chiou, S. Y. & Ou, K. L. Ceram. Int. 2013, 39, 3809-3816.
- 76. Irwansyah, F. S.; Amal, A. I.; Hadisantoso, E. P.; Noviyanti, A. R.; Eddy, D. R. & Risdiana, R. Results Chem. 2025, 13, 101932.
- 77. Zhang, C.; Yang, J.; Quan, Z.; Yang, P.; Li, C.; Hou, Z. & Lin, J. Cryst. Growth Des. 2009, 9, 2725-2733.

- 78. Hashim, N. C. & Nordin, D. Mater. Today Proc. 2019, 19, 1562-1571.
- 79. Shah, F. A.; Ruscsák, K. & Palmquist, A. Bone Res. 2019, 7, 15.
- 80. Han, JH.; Pack, S. P. & Chung, S. Korean J. Chem. Eng. 2020, 37, 891-897.
- 81. Standard Practice for Assessment of Hemolytic Properties of Materials regulated by Advancing Standards Transforming Markets (ASTM standard F756-00) https://store.astm.org/f0756-17.html.
- 82. Barbosa, A. A.; Júnior, S. A.; Mendes, R. L.; de Lima, R. S. & de Vasconcelos Ferraz, A. Mater. Sci. Eng. C. 2020, 116, 111227.
- 83. Radha, G.; Balakumar, S.; Venkatesan, B. & Vellaichamy, E. Mater. Sci. Eng. C. 2015, 50, 143-150.
- 84. Liu, T.; Bai, R.; Zhou, H.; Wang, R.; Liu, J.; Zhao, Y. & Chen, C. RSC Adv. 2020, 10, 7559-7569.
- 85. van Oeveren, W. Scientifica, 2013, 2013, 392584.
- 86. Yun, S. H.; Sim, E. H.; Goh, R. Y.; Park, J. I. & Han, J. Y. Biomed. Res. Int. 2016, 2016, 9060143.
- 87. Weber, M.; Steinle, H.; Golombek, S.; Hann, L.; Schlensak, C.; Wendel, H. P. and Avci-Adali, M. Front. Bioeng. Biotechnol. 2018, 6, 99.
- 88. Xu, L. C.; Bauer, J. W. & Siedlecki, C. A. Colloids Surf. B: Biointerfaces. 2014, 124, 49-68.
- 89. Kalathottukaren, M. T. & Kizhakkedathu, J. N. Woodhead Publishing, 2018, 29-49.
- 90. Shanmugam, P. S. T; Thangaraju, P.; Palani, N. & Sampath, T. Medical device guidelines and regulations handbook, Springer (Eds). 2022.
- 91. Holling, N.; Lednor, D.; Tsang, S.; Bissell, A.; Campbell, L.; Nzakizwanayo, J.; Dedi, C.; Hawthorne, J. A.; Hanlon, G.; Ogilvie, L. A.; Salvage, J. P.; Patel, B. A.; Barnes, L. M. & Jones, B. V. Journals. Asm. Org. 2014, 82, 1616-1626.
- 92. Fernández-Delgado, M.; Duque, Z.; Rojas, H.; Suárez, P.; Contreras, M.; García-Amado, M. A. & Alciaturi, C. Ann. Microbiol. 2015, 65, 1401-1409.

- 93. Klausen, M.; Heydorn, A.; Ragas, P.; Lambertsen, L.; Aaes-Jørgensen, A.; Molin, S. & Tolker-Nielsen, T. Mol. Microbiol. 2003, 48, 1511-1524.
- 94. Mojahedian, M.; Fahimipour, F.; Larsen, K. L.; Kalantar, M.; Bastami, F. & Omatali, N. J. Ceram. Process. Res. 2016, 17, 1138-1142.
- 95. Pal, K.; Pal, S. Mater. Manuf. Process. 2006, 21, 325-328.
- 96. Estrada, O.; Alvarado-Castillo, C.; Fernández, A.; López, M.; Romero-Vecchione, E.; Vásquez, J.; Méndez, J.; Conde, D.; Cardozo, A. 2009, 5, 219-225.
- 97. Suárez, P.; Gutiérrez, A. V.; Salazar, V.; Puche, M. L.; Serrano, Y.; Martínez, S.; González, G.; Fernández-Delgado, M. Lett. Appl. Microbiol. 2020, 70, 372-379.